Entrainment of a Population of Synthetic Genetic Oscillators

Octavio Mondragón-Palomino,[1] Tal Danino,[1] Jangir Selimkhanov,[1,2] Lev Tsimring,[2,3]* Jeff Hasty[1,2,3,4]*†

Biological clocks are self-sustained oscillators that adjust their phase to the daily environmental cycles in a process known as entrainment. Molecular dissection and mathematical modeling of biological oscillators have progressed quite far, but quantitative insights on the entrainment of clocks are relatively sparse. We simultaneously tracked the phases of hundreds of synthetic genetic oscillators relative to a common external stimulus to map the entrainment regions predicted by a detailed model of the clock. Synthetic oscillators were frequency-locked in wide intervals of the external period and showed higher-order resonance. Computational simulations indicated that natural oscillators may contain a positive-feedback loop to robustly adapt to environmental cycles.

One focus of synthetic biology is the genome-scale synthesis of DNA for the creation of novel cell types (*1*). This approach could lead to cells with highly reduced genomic complexity, as genes that govern the ability to adapt to multiple environments are eliminated to construct specialized organisms for biotechnology and basic research. Another branch of synthetic biology involves the engineering of gene circuits, in which mathematical tools are developed to systematically design and construct circuits from a standardized list of biological parts (*2*–*11*). The engineering approach allows the construction of circuits that mimic natural networks to understand the design principles that underlie a given network motif (*12*, *13*). In this context, molecular clocks are a natural application of synthetic biology, and recent efforts have led to a deeper understanding of the robustness and reliability of time-keeping at the intracellular level (*3*, *7*, *8*, *10*).

Almost all organisms use molecular clocks to keep their physiology and behavior in synchrony

[1]Department of Bioengineering, University of California, San Diego, La Jolla, CA 92093–0412, USA. [2]San Diego Center for Systems Biology, University of California, San Diego, La Jolla, CA 92093–0412, USA. [3]BioCircuits Institute, University of California, San Diego, La Jolla, CA 92093–0402, USA. [4]Molecular Biology Section, Division of Biological Sciences, University of California, San Diego, La Jolla, CA 92093–0368, USA.

*These authors contributed equally to this work.
†To whom correspondence should be addressed. E-mail: hasty@ucsd.edu

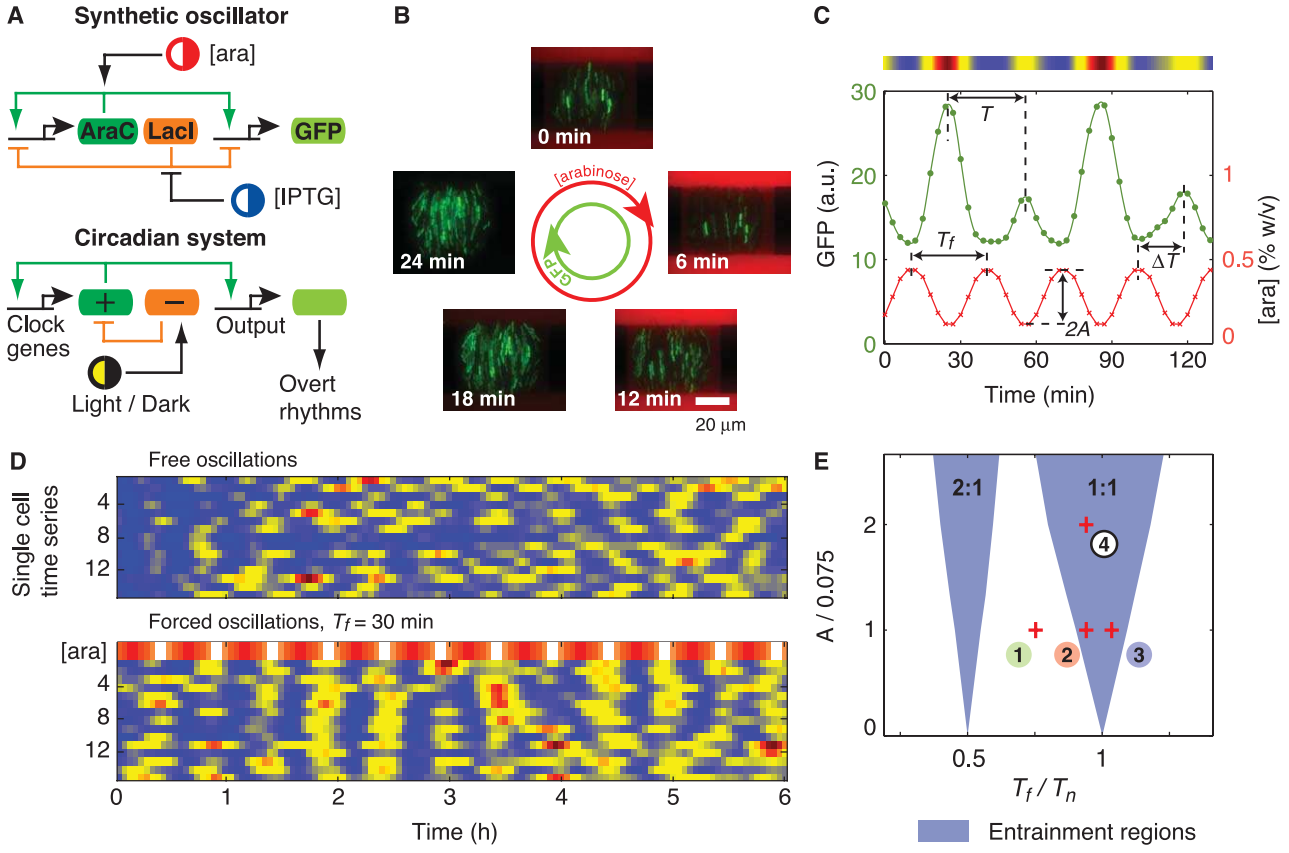

Fig. 1. We use single-cell data from time-lapse fluorescence experiments to investigate the entrainment of a synthetic oscillator. (**A**) Architectures of eukaryotic circadian clocks and bacterial synthetic oscillators contain positive- and negative-feedback loops that are sensitive to external stimuli. (**B**) Fluorescence images from a time-lapse experiment show coherent GFP oscillations (green) in a colony of single-cell oscillators subject to a 30-min cycle of arabinose (red) (movie S1). (**C**) Fluorescence time series of a single-cell oscillator (green). The concentration of arabinose (red) changes sinusoidally according to $[ara](t) = 0.3 + A\sin(2\pi t/T_f)$ [percent weight/volume (% w/v)], with A = 0.15% and T_f = 30 min. The intensity plot above the graph corresponds to the cell trace. a.u., arbitrary units. (**D**) Fluorescence intensity plots of free-running and forced oscillators. Each row in the two panels represents a single-cell trace. The top row of the forced set represents the modulated concentration of arabinose (A = 0.15%). (**E**) Entrainment regions indicate which forcing periods (T_f) and amplitudes (A) result in locking of the oscillator according to a deterministic model (SOM text). Entrainment of order 2:1 means that two oscillation peaks are observed for one peak of arabinose. T_n is the natural period of the oscillator. Images and cell traces shown in (B), (C) and [(D), forced oscillations] correspond to point 4. Points 1 to 3 signal some parameter values explored experimentally.

with their surroundings (*14*). Such coordination is mediated by entrainment, whereby a population of intracellular clocks oscillate in unison guided by a common external signal (*14*, *15*). Quantitative descriptions of entrainment that arise from the tight coupling of computational modeling and experimentation are challenging to develop because of the complexity of the underlying gene-regulatory networks, in which dozens of genes are involved in the core clocks and hundreds more act as their modifiers (*16*). Moreover, a quantitative description of inherently stochastic circadian clocks requires abundant long-term single-cell data, which are technically challenging to obtain (*17*–*19*). We combined synthetic biology, microfluidic technology (*20*), and computational modeling to investigate the fundamental process of entrainment at the genetic level.

We used a synthetic oscillator that has coupled positive- and negative-feedback loops that are characteristic of many circadian gene-regulatory networks (Fig. 1A) (*7*). The green fluorescent protein (GFP) was used as a readout of the transcriptional activation state of the promoter that drives the expression of the oscillator genes. We stimulated the expression of the oscillator genes (*araC* and *lacI*) by periodically modulating the concentration of the transcriptional inducer arabinose, which acts on the positive-feedback loop. Such stimulation is referred to as the forcing of the oscillator. To generate long-term single-cell data for comparison with computational modeling, we constructed microfluidic devices in which bacterial colonies can grow exponentially for at least 150 generations (fig. S1) (*21*). For each experimental run, we tracked the phase of the oscillations with respect to the arabinose signal in ~1600 cells (Fig. 1B and movies S1 and S6) (*21*). The period of oscillations T was measured as the peak-to-peak interval in the GFP fluorescence time series. The phase difference between an oscillator and the arabinose signal was calculated as $\Delta\phi = 2\pi\Delta T/T_f$, where T_f is the period of the forcing signal and ΔT is the measured time interval between a crest of arabinose and the immediate following peak of GFP fluorescence (Fig. 1C). Entrainment of the intracellular oscillations to the chemical signal was readily identified from color density maps of the fluorescence trajectories (Fig. 1D); by taking crests of GFP fluorescence as a marker of the phase, one can see that whereas in the autonomous set single cells are not always in phase with respect to each other, maxima in the forced colony occur almost simultaneously during most of the run.

The entrainment of any self-sustained oscillator can be characterized by comparing its natural period (T_n) and phase (ϕ) to those of the external signal. When T_f is sufficiently close to the natural period of the oscillator, the oscillator can be entrained. In the entrainment regime, the period of the oscillator T is equal to T_f, and the phase difference $\Delta\phi$ between the oscillator and the forcing signal is fixed. In the plane defined by the period and amplitude of the external signal (T_f, A), a triangular region near $T_f/T_n = 1$ indicates where the oscillator is entrained [Fig. 1E and supporting online material (SOM)

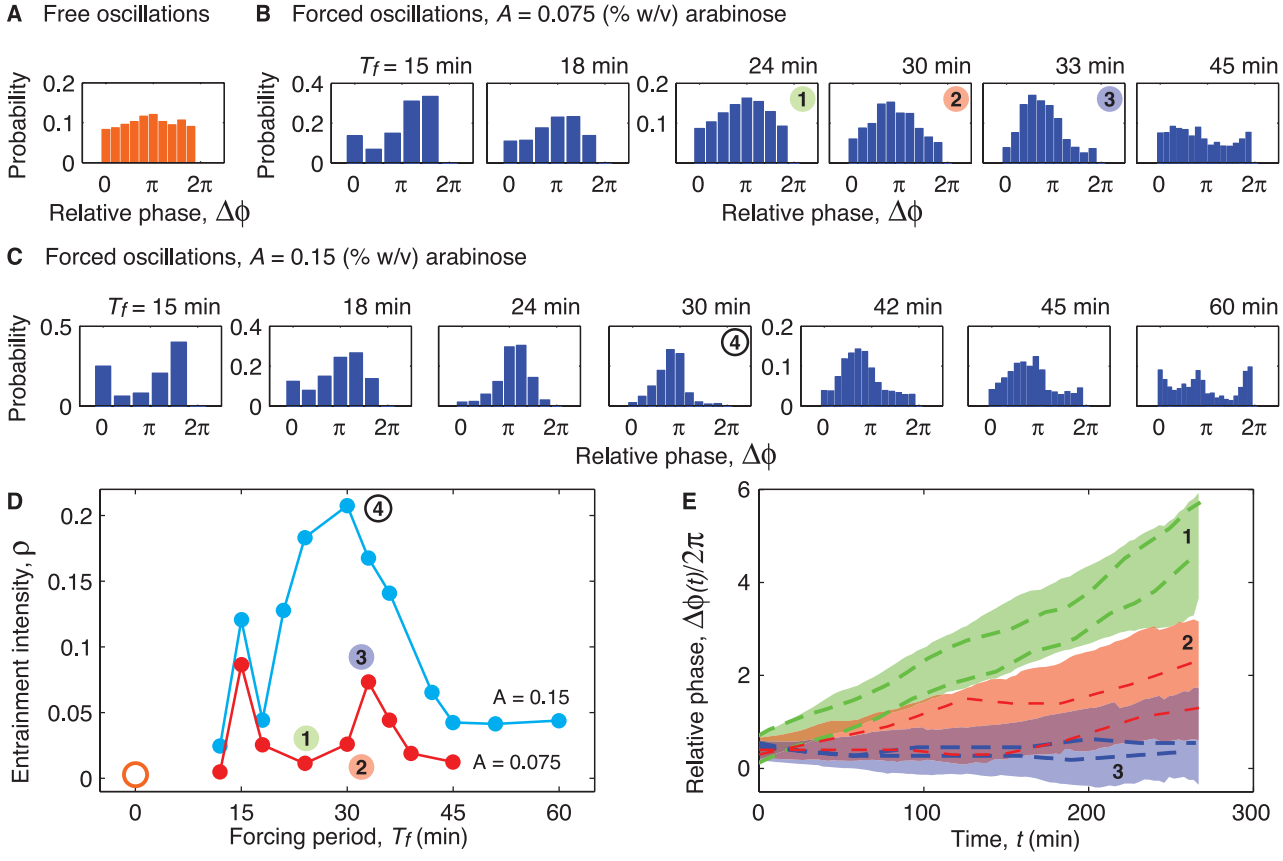

Fig. 2. Probability distributions of the relative phase of oscillators with respect to the external signal allow the detection of entrainment. (**A**) Probability distribution of the relative phase of free-running oscillators in several colonies with respect to a virtual sinusoidal signal of period T_f = 30 min. Constant concentrations of inducers were used ([IPTG] = 2 mM, [ara] = 0.3%). (**B**) Probability distributions of the relative phase for multiple forcing periods with amplitude A = 0.075% (w/v). In the presence of the external stimulus, distributions acquired a preferred phase that depends on the forcing period T_f. (**C**) Same as (B) for stronger forcing with A = 0.15%. Increased amplitude sharpens the peaks of the relative phase distributions with respect to those for A = 0.075% as in T_f = 15, 30, and 45 min. (**D**) Intensity of entrainment as a function of the forcing period for the two values of the forcing amplitude. In each curve, two peaks centered near $T_f \sim T_n$ = 31.8 min and $T_f \sim T_n/2$ = 15.9 min reveal the intervals of T_f where the phase is locked to the arabinose input. For free-running oscillators, ρ is nearly zero (orange open circle). (**E**) Relative phase as a function of time for three experiments shown in (B). Colored regions correspond to ±SD around the mean phase drift. Dashed lines indicate representative single-cell traces.

text]. Entrainment may also occur near other rational values of T_f/T_n. Collectively, these regions are known as Arnold tongues. The order of locking in each region is indicated by the ratio *n*:*m*, which denotes that *m* oscillations of the clock correspond to *n* oscillations of the arabinose signal. We computed the tongues for entrainment of order 1:1 and 2:1 with a deterministic model of the synthetic oscillator (*7*), in which we periodically modulated the arabinose concentration.

To experimentally map the entrainment regions, we first determined the natural period of the oscillator by tracking the expression of GFP of cells at constant inducer concentrations (movie S2). Because the oscillators are not synchronized with respect to each other, their phases are uniformly distributed between 0 and 2π (Fig. 2A). Similar to its naturally occurring counterparts (*17*, *18*, *22*), the synthetic oscillator shows considerable fluctuations (Fig. 3A). Given the natural period of ~32 min, we varied the period of the arabinose concentration from 6 to 60 min for two values of the amplitude. Coherent oscillations emerged over a range of periods that bounded the natural period (movie S3). Phase-locking was characterized by a narrow peak in the phase distribution (*23*), which became difficult to discern as the period of the signal diverged from the natural period but reappeared as the forcing period approached half of the natural period (Fig. 2B and movie S4). An increase in the forcing amplitude by a factor of 2 led to sharper distributions of the relative phase (Fig. 2C and movies S1 and S5). To quantify the degree of phase-locking, we used an entropy-based index (ρ) to characterize the width of the distributions (*23*); wider distributions imply less phase-locking and lead to smaller values of ρ (SOM text). Accordingly, maxima of the entrainment index appeared at both the natural period and half of the natural period (Fig. 2D).

The flattening of phase distributions and the decay of the phase-locking index around T_f/T_n = 1/2,1 indicates the breaking of entrainment. To investigate this transition in more detail, we examined the dynamics of the oscillation phase relative to the forcing signal in single cells. We chose three values of the forcing period that cross the left boundary of the computed main Arnold tongue (Fig. 1E). We used peak positions to determine the phases of the arabinose signal $\phi_{ara}(t)$ and single-cell oscillations $\phi_c(t)$, and we calculated their difference $\Delta\phi(t) = \phi_{ara}(t) - \phi_c(t)$ (Fig. 2E). Near the center of the entrainment region (T_f = 33 min), $\Delta\phi$ for most oscillators was nearly constant (Fig. 2E, blue shaded region and curves). Toward the left boundary of the tongue (T_f = 30 min), there is a slow mean phase drift with a broad distribution (Fig. 2E, red shaded area and curves); some cells exhibit phase drift (with an evidence of occasional phase slips), whereas other cells are still phase-locked. Finally, between the two Arnold tongues (T_f = 24 min), the rate of phase drift was even faster and almost uniform because the phases of most oscillators did not lock to the arabinose signal (Fig. 2E, green shaded area and curves). The continuous phase drift indicates quasi-periodic behavior outside entrainment regions, which is observed in the computation of Arnold tongues (Fig. 1E and SOM text).

We also used period distributions to characterize the response of the oscillator (Fig. 3). Forcing periods close to both the natural period and half of the natural period reduce the spread of the period distribution in a manner similar to that observed with light pulses resetting peripheral clocks (*22*). For a lower amplitude of the arabinose signal, oscillators were entrained over an interval of periods that was consistent with the width of the 1:1 phase-locking regime determined with the use of the entropy-based measure (Figs. 2D and 3D). For a larger forcing amplitude, the 1:1 plateau extended over a larger interval of periods, and a 2:1 plateau indicated the presence of the higher-order resonance. Some of these distributions displayed two modes, which presumably indicated simultaneous occurrence of 1:1 and 2:1 frequency-locking.

Direct comparison between our experimental results and the computed Arnold tongues indicated that the locations of the experimental entrainment plateaux correspond closely to the regions where frequency-locking is predicted (Fig. 4A). The width of the plateau increased

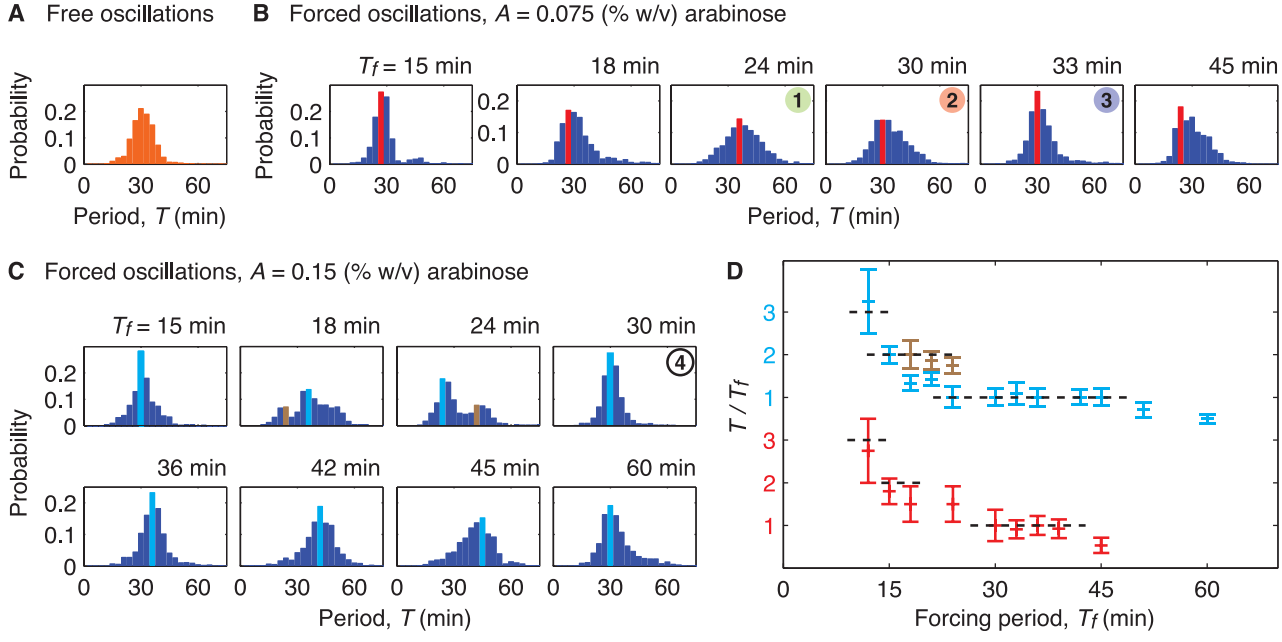

Fig. 3. Probability distributions of the period of oscillations allow us to find the forcing periods that lead to frequency-locking. (**A**) Probability distribution for the period of free-running oscillators in constant concentrations of inducers ($\overline{[IPTG]}$ = 2 mM, $\overline{[ara]}$ = 0.3%). In forcing experiments, the concentration of arabinose oscillates sinusoidally around $\overline{[ara]}$ = 0.3%. We defined the natural period as the mean period of free oscillations, T_n = 31.8 min with standard deviation δT = 5.7 min. (**B**) Probability distributions of the period for multiple values of the T_f with A = 0.075%. For T_f near T_n = 31.8 min or $T_n/2$ = 15.9 min, the dispersion of the period is the least. Red bars indicate the mode of the distributions. (**C**) Probability distributions of the period for multiple values of the forcing period with A = 0.15%. Period distributions for this higher amplitude can contain two modes (light blue and brown bars). (**D**) The ratio T/T_f as a function of T_f for the two forcing amplitudes, where T is the mode(s) of the period distributions. The intervals of the forcing period where $T/T_f \sim 1,2$ provided evidence for entrainment of order 1:1 and 2:1, respectively.

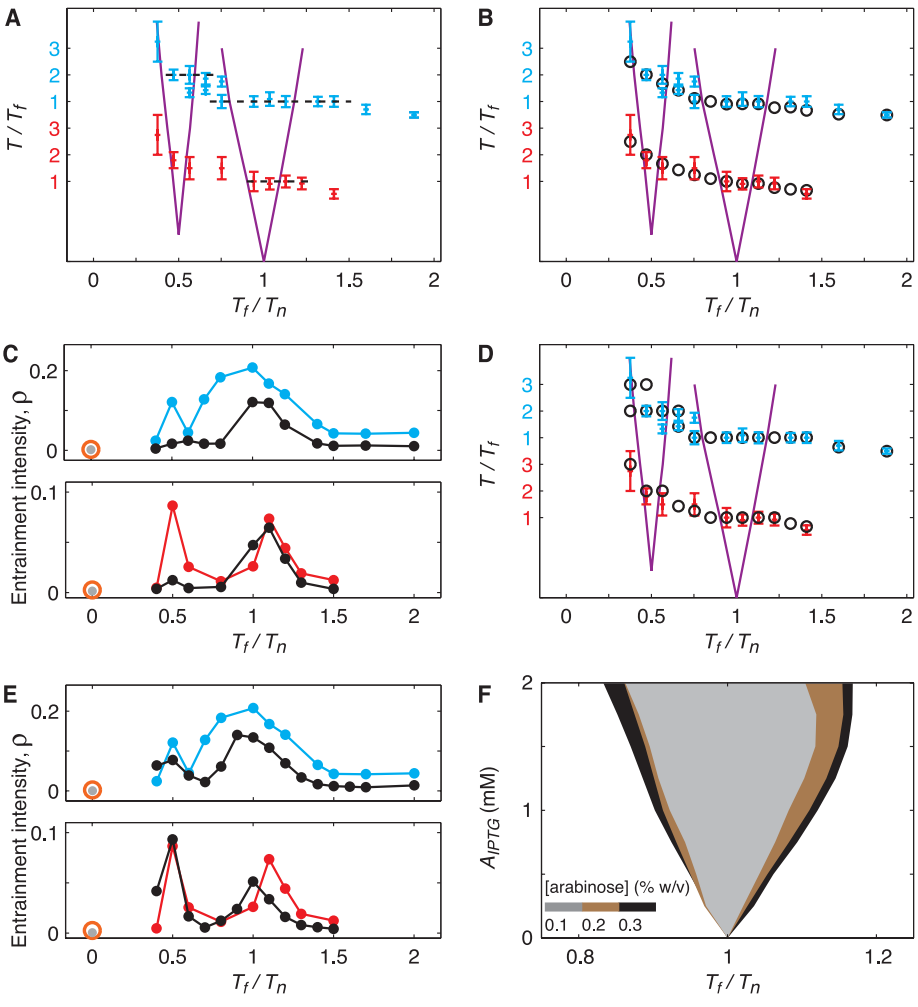

Fig. 4. Computational modeling shows that extrinsic sources are the dominant contribution to variability. Blue and red data points indicate experimental data for A = 0.075% and A = 0.15%, respectively. Error bars represent ±SD. (**A**) Experimental values of T/T_f alongside computed entrainment regions (purple lines), which are shifted with respect to each other to account for the gap between the T/T_f = 1 and T/T_f = 2. Entrainment was observed for T_f outside the computed entrainment areas. (**B** and **D**) Same as (A), along with the prediction for the ratio T/T_f (open circles) from a stochastic model (B) and from a deterministic model with distributed parameters in a set of 550 oscillators (D). Unlike the oscillator subject to intrinsic noise (B), the oscillator with distributed kinetic parameters became phase-locked outside computed entrainment regions (D). The ratio T/T_f diverges from 1 or 2 outside Arnold tongues (B). (**C** and **E**) Experimental values of the intensity of entrainment ρ alongside the prediction (black circles) from a stochastic model (C) and a deterministic model with distributed parameters in a set of 550 oscillators (E). Intrinsic variability destroys the resonance around T_f/T_n = 0.5 (C), whereas the model with distributed parameters captures it (E). (**F**) Main entrainment region for forcing with a sinusoidal IPTG signal of amplitude A_{IPTG} for three concentrations of arabinose from a deterministic model (SOM text). When the oscillator is forced through its negative-feedback loop (Fig. 1A), the range of entraining frequencies increases with the constant arabinose concentration (strength of positive-feedback loop).

with the amplitude of the forcing signal, as follows from classical theory (*24*). However, the experimental entrainment regions were consistently wider than the computed Arnold tongues. The major discrepancy between the naive model and experiment is that the model assumes that all oscillators are identical and have the same natural period, whereas the bacterial colony exhibits a broad distribution of periods (Fig. 3A).

The observed variability of the oscillatory dynamics can be attributed to both intrinsic and extrinsic origins (*25*). We incorporated both sources of variability into our model because it is difficult to ascertain which one dominates. We used a Gillespie algorithm (*26*) to simulate the stochastic model of the oscillator network with intrinsic noise only (the kinetic parameters of all oscillators were set to be identical). Although the simulated distributions appeared similar to experimental data (figs. S2 to S5), the stochastic model did not account for the higher-order (2:1) resonance entrainment, the period bimodality, or the wider entrainment regions (Fig. 4, B and C, black circles, and figs. S2 to S5). We therefore modeled extrinsic variability by varying the kinetic parameters of the deterministic model across a population of 550 cells. In particular, we assumed that the rates of transcription, translation, enzymatic degradation by proteases, and plasmid copy numbers were normally distributed around their nominal values. Using a coefficient of variation (CV) of 0.15, close to CV = 0.18 of the experimental probability distribution of the free-running period, we obtained good agreement between the modes of simulated and experimental period distributions (Fig. 4D, black circles, and figs. S7 and S9). Accordingly, the distributions of the relative phase and the peaks in the curves for the intensity of phase-locking were comparable (Fig. 4E and figs. S6 and S8). Deterministic simulations with randomized parameters accounted for the width of both the 1:1 and 2:1 entrainment regions. Simulations also reproduced peaks in some bimodal period distributions (figs. S7 and S9).

These results can be readily understood in the context of the phase dynamics. For fixed concentrations of arabinose and isopropyl-β-D-thiogalactopyranoside (IPTG), the natural period of the oscillator T_n is a function of the parameters of the model—for instance, the rates of transcription, translation, enzymatic degradation, and of the ratio of activator to repressor plasmids. Therefore, variability in these parameters will lead to the observed variability in the periodicity of free-running oscillations (Fig. 3A). Each individual oscillator will respond differently to the forcing arabinose signal, and depending on its natural frequency, it may or may not entrain. If the natural-frequency distribution occupies an interval of a given width, the entrainment interval will broaden by the same amount (SOM text). Moreover, the broad distribution of natural frequencies of oscillators explains the occurrence of bimodal period distributions. If the forcing frequency is shifted with respect to the peak of the free-running frequency distribution, both the entrainment peak at T_f and the "free" peak at T_n may coexist.

Because circadian oscillators can be entrained by stimuli that act on different components (*27*), we explored the entrainment of the oscillator through the periodic modulation of the concentration of IPTG (Fig. 1A). We did this through deterministic simulations of the model, in which arabinose was kept constant and the concentration of IPTG oscillated sinusoidally (SOM text). We found a similar behavior to forcing with arabinose, with a main entrainment region that widened with the amplitude of change in IPTG concentration. Because the concentration of arab-

inose defines the strength of the positive feedback through the AraC-DNA binding rate, we used different values to explore how entrainment depends on the strength of positive feedback. Lower concentrations of arabinose yielded narrower Arnold tongues (Fig. 4F). In other words, a weaker positive loop makes the oscillator less entrainable.

We have shown how the coupling of synthetic biology, microfluidic technology, and computational modeling can be used to explore the complex process of entraining molecular clocks. Our results indicated that the positive-feedback loop widens the entrainment region for single cells, providing insight into the possible role of positive feedback in the robust adaptation of variable clocks to complex environments (*28*). The observation of higher-order entrainment and the wider entrainment regions allowed us to discriminate intrinsic sources in favor of extrinsic noise as the main contribution to stochastic variability in computational modeling of the clock. Other manifestations of strong cell-cell variability in gene networks have been quantified (*29*). Although cell-cell variability may be deleterious to biological function, variable entrainment properties across a population may provide increased flexibility to the various signals that reset clocks. This may be relevant in the context of multicellular circadian systems where uncoupled peripheral oscillators display variability and are exposed to multiple signals (*17*, *18*, *22*, *30*). Other properties at the cell and tissue level have been found to contribute to the flexibility of circadian clocks; recent work found an effect of the strength of coupling between cell clocks on the range of entrainment in mammalian circadian clocks (*19*).

References and Notes

1. D. G. Gibson *et al*., *Science* **329**, 52 (2010); 10.1126/science.1190719.
2. T. S. Gardner, C. R. Cantor, J. J. Collins, *Nature* **403**, 339 (2000).
3. M. B. Elowitz, S. Leibler, *Nature* **403**, 335 (2000).
4. J. Hasty, D. McMillen, J. J. Collins, *Nature* **420**, 224 (2002).
5. S. Basu, Y. Gerchman, C. H. Collins, F. H. Arnold, R. Weiss, *Nature* **434**, 1130 (2005).
6. D. Endy, *Nature* **438**, 449 (2005).
7. J. Stricker *et al*., *Nature* **456**, 516 (2008).
8. M. Tigges, T. T. Marquez-Lago, J. Stelling, M. Fussenegger, *Nature* **457**, 309 (2009).
9. A. Tamsir, J. J. Tabor, C. A. Voigt, *Nature* **469**, 212 (2011).
10. T. Danino, O. Mondragón-Palomino, L. Tsimring, J. Hasty, *Nature* **463**, 326 (2010).
11. C. Grilly, J. Stricker, W. L. Pang, M. R. Bennett, J. Hasty, *Mol. Syst. Biol.* **3**, article 127 (2007).
12. D. Sprinzak, M. B. Elowitz, *Nature* **438**, 443 (2005).
13. S. Mukherji, A. van Oudenaarden, *Nat. Rev. Genet.* **10**, 859 (2009).
14. D. Bell-Pedersen *et al*., *Nat. Rev. Genet.* **6**, 544 (2005).
15. C. H. Johnson, J. A. Elliott, R. Foster, *Chronobiol. Int.* **20**, 741 (2003).
16. E. E. Zhang, S. A. Kay, *Nat. Rev. Mol. Cell Biol.* **11**, 764 (2010).
17. D. K. Welsh, S. H. Yoo, A. C. Liu, J. S. Takahashi, S. A. Kay, *Curr. Biol.* **14**, 2289 (2004).
18. S. H. Yoo *et al*., *Proc. Natl. Acad. Sci. U.S.A.* **101**, 5339 (2004).
19. U. Abraham *et al*., *Mol. Syst. Biol.* **6**, 438 (2010).
20. G. M. Whitesides, E. Ostuni, S. Takayama, X. Jiang, D. E. Ingber, *Annu. Rev. Biomed. Eng.* **3**, 335 (2001).
21. Materials and methods are available as supporting material on *Science* Online.
22. A. J. Carr, D. Whitmore, *Nat. Cell Biol.* **7**, 319 (2005).
23. P. Tass *et al*., *Phys. Rev. Lett.* **81**, 3291 (1998).
24. A. Pikovsky, M. Rosenblum, J. Kurths, *Synchronization: A Universal Concept in Nonlinear Sciences* (Cambridge Univ. Press, Cambridge, 2003).
25. P. S. Swain, M. B. Elowitz, E. D. Siggia, *Proc. Natl. Acad. Sci. U.S.A.* **99**, 12795 (2002).
26. D. Gillespie, *J. Phys. Chem.* **81**, 2340 (1977).
27. C. E. Boothroyd, H. Wijnen, F. Naef, L. Saez, M. W. Young, *PLoS Genet.* **3**, e54 (2007).
28. D. A. Rand, B. V. Shulgin, D. Salazar, A. J. Millar, *J. R. Soc. Interface* **1**, 119 (2004).
29. E. Fischer-Friedrich, G. Meacci, J. Lutkenhaus, H. Chaté, K. Kruse, *Proc. Natl. Acad. Sci. U.S.A.* **107**, 6134 (2010).
30. C. Dibner, U. Schibler, U. Albrecht, *Annu. Rev. Physiol.* **72**, 517 (2010).

Acknowledgments: This work was supported by the National Institutes of Health and General Medicine (grant R01GM69811), the San Diego Center for Systems Biology (grant P50GM085764), and CONACyT (Mexico, grant 184646 to O.M.-P.). Single-cell data obtained from automated tracking and lineage reconstruction is available online at http://biodynamics.ucsd.edu/downloads.

Supporting Online Material

www.sciencemag.org/cgi/content/full/333/6047/1315/DC1
Materials and Methods
SOM Text
Figs. S1 to S9
References
Movies S1 to S6

9 March 2011; accepted 26 July 2011
10.1126/science.1205369

Supporting Online Material for

Entrainment of a Population of Synthetic Genetic Oscillators

Octavio Mondragón-Palomino, Tal Danino, Jangir Selimkhanov,

Lev Tsimring, Jeff Hasty.

Correspondence to: hasty@ucsd.edu

Contents

Materials and Methods.

Oscillator strain.

The dual-feedback oscillator is described in full detail in (*1*). Briefly, a cycle of the oscillator has two stages, dominated by either protein production or enzymatic degradation. The first stage is a positive feedback driven burst of mRNA from the clock genes *lacI* and *araC*, which goes on until enough LacI tetramer repressor accumulates and transcription is turned off, setting the conditions for the second phase where the activator and repressor proteins are enzymatically degraded. Protein degradation brings the system back to a state where a new transcription burst can occur. The time necessary to complete a cycle depends on the magnitude of the activation burst, which is roughly proportional to the induction level of the promoter. Therefore, the natural period of oscillations T_n can be externally tuned through the concentrations of inducers Arabinose and IPTG.

For this work we used the double feedback oscillator strain JS011 (*1*). In this strain the genetic oscillator is contained in two plasmids. The activator and reporter modules are on a derivative of pZE24, a medium-copy ColE1 plasmid, and the repressor module is on a derivative of pZA14, a lower-copy p15A plasmid. These plasmids are transformed into $\Delta araC \Delta lacI$ *E. coli* to obtain JS011 cells.

Microfluidics and microscopy

In the context of synthetic and cell biology, microfluidic devices have been used to obtain abundant dynamic data by lengthening the *in chip* life of microbes (*2–6*). In these designs cells are constrained to microscopic cavities of variable geometry where they are continuously supplied with nutrients. In the case of bacterium *E. coli*, our group and others realized that the mechanical interactions among bacteria and between bacteria and the walls of the micro-cavities leads

to cell spatial ordering (*7, 8*) (Movie S1). Moreover, we previously developed a microfluidic switch that allows the generation of chemical signals of any shape (*5*).

We built on this work by developing a microfluidic device where bacterial colonies can grow for long periods of time in a dynamic and precisely controlled environment (Fig. S1). The device consists of two parts: a trapping region and a dynamic switch. In the trapping region there are 48 rectangular cell chambers distributed in 4 columns. A cell chamber is a rectangular cavity with dimensions 40x50x0.95 μm^3, with the long sides open to the flow of medium. Since *E. coli* cells have a $\sim$1μm diameter, a trap allows focused observation of the $\sim$400 confined cells. The striped arrangement of cells inside small traps facilitates the exchange of nutrients, inducers and waste between the colony and the surrounding flow. The design also allows continuous discharge of cells into the flow, which carries them outside the device (Movie S1). In the dynamic switch, media flowing in from ports I and B (for Inducer and Background) are mixed to generate the modulated signal of inducers. During experiments, the concentrations of small molecules in medium I were $[IPTG] = 2$ mM and $[Ara] = 0.3{+}A$ %, and in the background medium B $[IPTG] = 2$ mM and $[Ara] = 0.3{-}A$ %. Therefore, by changing the hydrostatic pressure at ports I and B sinusoidally we changed the proportion of media I and B in the total flow. Media mixed by diffusion in the long and narrow channel leading from the switch to the trapping region, obtaining the concentration profiles of the signal $[Ara](t) = 0.3 + A\sin(2\pi t/T_f)$ % and $[IPTG] = 2$ mM.

In preparation for experiments JS011 cells were cultured overnight in LB medium with antibiotics (kanamycin at 100 μg/mL, ampicillin at 100μg/mL). The next day cells are passed into 200 mL of fresh medium in a 1000-fold dilution with antibiotics and average concentrations of inducers ($[IPTG] = 2$ mM, $[Ara] = 0.3$ %). Cells were grown until they reached an OD_{600} of 0.2-0.25. This culture was centrifuged and cells were resuspended in 1.5 mL of fresh medium supplemented with 0.075 % Tween 20 (Sigma-Aldrich), antibiotics and average concentrations

of inducers. Cells were introduced to the device from the cell port (C). The hydrostatic pressure at ports W1 and W2 was set so that most cells flowed through the trapping region into W2. No cells were allowed to flow into the dynamic switch area to avoid contamination of the media. Cells were loaded into the traps by gentle flicking of the fluidic line that delivered cell suspension from the reservoir to the chip. To supply loaded cells with media, the hydrostatic pressure at ports C, W1 and W2 was adjusted so that port C became the recipient of the trapping region flow-through and of water flowing from port W1. Water diluted media coming into port C, delaying the clogging of the port by cells. Finally, in order to guarantee oscillators were out of phase before delivering the modulated arabinose signal, cells were allowed to grow inside the traps for 2-3 hours in a constant environment with average inducer concentrations.

In each experiment, the microfluidic device was mounted to the stage of the microscope and primed using a solution of 0.1 % Tween 20 surfactant in water to reduce surface tension and improve wetting. Priming of the device was also necessary to remove all air from the microfluidic channels. This prevented bubble formation when fluid reservoirs were connected to the device inlets and cells were loaded. Culture temperature was maintained at 37^o C using a plexiglas incubation chamber. Images were collected at 100x magnification at intervals of 30 s for phase contrast and 3 min for GFP and MCherry fluorescence. Exposure times were chosen to prevent photobleaching and phototoxicity of cells (100 ms phase contrast, 500 ms GFP, 80 ms MCherry).

Data analysis

Ordered bacterial monolayers facilitated the automated tracking of cells and lineage reconstruction. Starting with the original sequence of brightfield images, we cropped each image such that only the cells inside the chamber were visible. We corrected for the positional drift that tends to occur in longer experiments by tracking the location of the frame in the original

images. Any out-of-focus images were replaced with a copy of the preceding brightfield image (happens rarely). Potential cell objects were extracted from the cropped images by automatic segmentation by a modified Otsu filter, user preset thresholding, and morphological operations completed in MATLAB (2009b, The MathWorks, Natick, MA). The Otsu threshold filter was used to obtain the background image containing all of the cell objects. Next, morphological opening, erosion, and dilation were applied to the background image to obtain cell object seeds. Using the background and object seed images, CellProfiler(TM) subfunction was utilized as a propagation algorithm to extract individual cell objects. Regionprops command was then employed to collect area, centroid location, and pixel information about each cell object. The goal of cell tracking was to track a cell object from one time lapse image to the next.

Using MATLAB, this was accomplished through a three step process. First, under the assumption that cells did not shift considerably between consecutive time lapse images, two successive images were overlaid and cell objects were matched up based on pixel overlap and distance between centroids. Matches were satisfied based on a one-to-one correspondence. In case of cell division, we were able to match only one of the two daughter cell objects to the mother cell object. In the second step of the cell tracking procedure, division events were identified based on significant reduction in the size of an object from one image to the next. The second daughter cell object, which did not have a matching cell object after the first tracking step, was determined based on pixel overlap and distance from the mother cell object. In the final tracking step, all of the matched objects from the two successive images were removed and any still unmatched objects were reassessed based on pixel overlap and centroid distance. Single cell fluorescence was calculated by averaging the corresponding object pixel values in fluorescence images. We applied Savitzky-Golay smoothing filter to the fluorescence trajectories before extracting the periods. We defined the period length as the time distance between two successive peaks. Using image dilation we identified individual peaks and the respective

troughs for each peak. Amplitudes of each peak were taken as the fluorescence difference between the troughs and the peak. The peaks whose amplitudes fell below a predetermined cutoff value, were removed.

Each peak in single cell trajectories marks the increase of the phase by 2π (or one cycle). Using linear interpolation between peak times, we obtained phase trajectories for every cell. Using a similar approach we calculated the phase trajectory of the input signal. By taking the difference between the signal and cell phase trajectories, we obtained the phase difference between the input signal and each cell trajectory as a function of time. Single cell trajectories that did not start simultaneously with the signal where shifted to the origin of the time coordinate.

The single cell data obtained from automated tracking and lineage reconstruction is available online at http://biodynamics.ucsd.edu/downloads. Each folder contains three types of MATLAB mat files. The file **trajectories_∗Ara_∗Min_xy∗.mat** contains fluorescent trajectory data (fluorescence, area, position) with rows representing cells and columns representing time points (3min spacing). The name of the file specifies strength of the driving signal (A % (w/v)), period of the driving signal (T_f, 0Min refers to no free running data), and the number of the colony (up to 4). The file **MaxIntensityArray_0.15.mat** contains a matrix for the cutoff for the maximum fluorescence value with rows representing signals with different entrainment period (0min not included), and columns representing trap number. The file **SignalArray_0.15.mat** contains a matrix with columns representing time series of arabinose signals (0min not included) and rows representing time points (3min spacing).

Quantitative analysis

Entrainment regions

Any self-sustained oscillator can be characterized by three main parameters; the amplitude (A), natural frequency ($\omega_n = 2\pi/T_n$), and the phase (ϕ). In an autonomous regime, the phase grows linearly with time as $\phi_n = \omega_n t$. However, when an oscillator is driven by a periodic signal with frequency ω_f (or period $T_f = 2\pi/\omega_f$), and phase $\phi_f = \omega_f t$, its phase ϕ is perturbed according to the phase equation $d\Delta\phi/dt = \omega_n - \omega_f + \epsilon Q(\Delta\phi)$ (*9*). In this equation, $\Delta\phi = \phi - \phi_f$ is the difference between the phase of the oscillator and the phase of the driving force, and the term $\epsilon Q(\Delta\phi)$ represents the effect of external perturbation with amplitude ϵ. Entrainment occurs if $\epsilon Q_{min} < \omega_f - \omega_n < \epsilon Q_{max}$, where Q_{min} and Q_{max} are the extremes of the 2π-periodic function $Q(\Delta\phi)$ (*9*). This condition defines a wedge in the plane (T_f, ϵ) near $T_f/T_n = 1$ which is known as the main Arnold tongue. When the oscillator is nonlinear, or the driving signal is non-sinusoidal, the entrainment may also occur near other rational values of T/T_f, however the corresponding higher-order Arnold tongues are much narrower. If the natural frequency distribution occupies the interval $[\omega_n - \Delta\omega, \omega_n + \Delta\omega]$, the entrainment interval will broaden to $\epsilon Q_{min} - \Delta\omega < \omega_f - \omega_n < \epsilon Q_{max} + \Delta\omega$.

Definition of the entrainment index ρ

The entrainment index is defined as $\rho = 1 - S/S_{max}$, where $S = -\sum_{k=1}^{N} P_k \ln P_k$ is the entropy of the discrete period distribution, P_k is the normalized occupancy of the k^{th} bin, N is the total number of bins, and $S_{max} = \ln N$ (*10*).

Computational modeling

Deterministic and stochastic computational models constructed in (*1*) were modified to include the periodic modulation of arabinose. The underlying set of biochemical reactions can be found in the supplementary information of (*1*). For all computational simulations the nominal values of kinetic constants where the same and as specified here: $b_a = b_r = 0.36$ min^{-1}, $\alpha = 35$, $k_{-a} = k_{-r} = 1.8$ min^{-1}, $t_a = 85$ min^{-1}, $t_r = 90$ min^{-1}, $d_a = d_r = 0.54$ min^{-1}, $k_{fa} = k_{fr} = 0.9$ min^{-1}, $k_{da} = k_{dr} = k_t = 0.018$ min^{-1} molecules^{-1}, $k_{-da} = k_{-dr} = k_{-t} = 0.00018$ min^{-1}, $k_l = 0.36$ min^{-1}, $k_{ul} = 0.18$ min^{-1}, $\gamma = 1080$ molecules/min, $c_e = 0.1$ molecules,$\lambda = 2.647$, $\epsilon = 0.2$, $Na = 50$, $Nr = 25$, $C_r^{max} = 0.2$ molecules^{-1}, $C_r^{min} = 0.01$ molecules^{-1}, $k_{r1} = 0.035$ mM, $b_1 = 2$, $C_a^{max} = 1$ molecules^{-1}, $C_a^{min} = 0$ molecules^{-1}, $k_{a1} = 3.5\%$, $k_{r2} = 1.8$ mM, $c1 = 2$,$b2 = 2$. [IPTG] is the IPTG concentration in mM, [ara] is the concentration of arabinose in % w/v.

We calculated the boundaries of the Arnold tongues numerically using the deterministic model of the oscillator. At every value of the driving amplitude we computed the time series of the concentration of AraC $a(t)$ and extracted the values $a_n = a(nT_f)$ separated by the driving period. They form iterations of the *return map* $a_{n+1} = F(a_n)$ associated with the continuous-time deterministic model. Within the main Arnold tongue, these iterates converge to a fixed point defined by condition $a_* = F(a_*)$. The 2:1 resonance tongue corresponds to a fixed point of the second iterate of the return map, $a_0 = F(F(a_0))$. The boundaries of the main Arnold tongue for a given value of the driving amplitude are manifested as bifurcation points at which the fixed point of the corresponding return map becomes unstable. Numerically, we calculated the coefficient of variation of the sequence of 100 iterations a_n (for the main tongue) and a_{2n} (for the 2:1 resonance) after the transients died out, and identified the bifurcation points by the values of the driving period at which the CV crossed the nominal threshold value 10^{-3}. In principle, there is a countable set of other higher-order Arnold tongues corresponding to

other $n : m$ resonances, however they are very narrow and difficult to identify, especially in experiment. Outside the Arnold tongues the phase of the oscillator is not locked to the phase of the driving signal. The continuous phase drift is the indication of the quasiperiodic behavior (*9*). Close to the boundaries of Arnold tongues, the phase drift is non-uniform in time: the intervals of almost constant phase difference are interrupted by periodic phase slips.

We used the stochastic model to simulate the forcing of the double-feedback oscillator when its components are subject to intrinsic noise only. At every value of the driving amplitude and period we computed time series of the number of AraC and LacI molecules. We smoothed them using a Savitsky-Golay filter and used a threshold value to distinguish true oscillation peaks from noise. From time series we obtained the period T and the relative phase $\Delta\phi$, which are defined in the same way as for the experimental fluorescence time series (see Fig. 1C). The resulting probability distributions of the period and relative-phase can be compared to our experimental results (Figs. S3-S6).

The deterministic model was also used to simulate the forced oscillations of individual oscillators in a colony of 550 cells where extrinsic noise is the only source of variability. To model this we assumed the copy-number of the activator and repressor plasmids (Na, Nr), the transcription and translation rates of AraC and LacI (b_a, t_a, b_r, t_r) and the rate of degradation (γ) of the ssrA tagged proteins by the ClpXP protease are distributed normally around their nominal values. The degradation of tagged proteins includes the monomer and oligomer forms of AraC and LacI in any folding state and in their free or DNA bound states. The coefficient of variation (CV$= \sigma/\mu$) of the distributions is set to CV$= 0.15$, which was chosen to best fit our experimental results and is close to the experimental probability distribution of the free-running period CV$= 0.18$.

At every value of the driving amplitude and period we computed time series of the concentration of AraC and LacI molecules. From time series we obtained the period T and the relative

phase $\Delta\phi$, which are defined in the same way as for the experimental fluorescence time series (see Fig. 1C). The resulting probability distributions of the period and relative-phase can be compared to our experimental results (Figs. S7-S10).

References and Notes

1. J. Stricker, *et al.*, *Nature* **456**, 516 (2008).

2. M. Bennett, J. Hasty, *Nature Reviews Genetics* **10**, 628 (2009).

3. A. Groisman, *et al.*, *Nature Methods* **2**, 685 (2005).

4. F. Balagaddé, L. You, C. Hansen, F. Arnold, S. Quake, *Science* **309**, 137 (2005).

5. M. Bennett, *et al.*, *Nature* **454**, 1119 (2008).

6. T. Danino, O. Mondragón-Palomino, L. Tsimring, J. Hasty, *Nature* **463**, 326 (2010).

7. H. Cho, *et al.*, *PLoS Biology* **5**, e302 (2007).

8. D. Volfson, S. Cookson, J. Hasty, L. Tsimring, *Proceedings of the National Academy of Sciences* **105**, 15346 (2008).

9. A. Pikovsky, M. Rosenblum, J. Kurths, *Synchronization: A universal concept in nonlinear sciences* (Cambridge Univ Pr, 2003).

10. P. Tass, *et al.*, *Physical Review Letters* **81**, 3291 (1998).

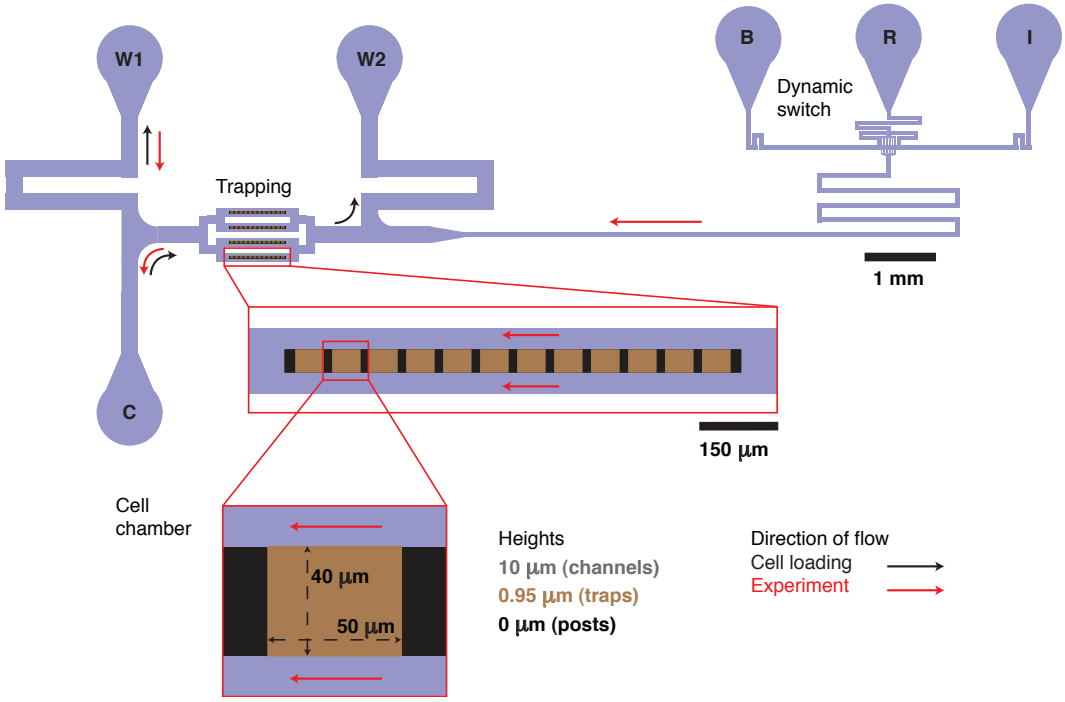

Fig. S1: Microfluidic device constructed for this study. The device consists of two parts: the signal generator (dynamic switch) and the trapping region, where 48 cell chambers host the same number of monolayer bacterial colonies.

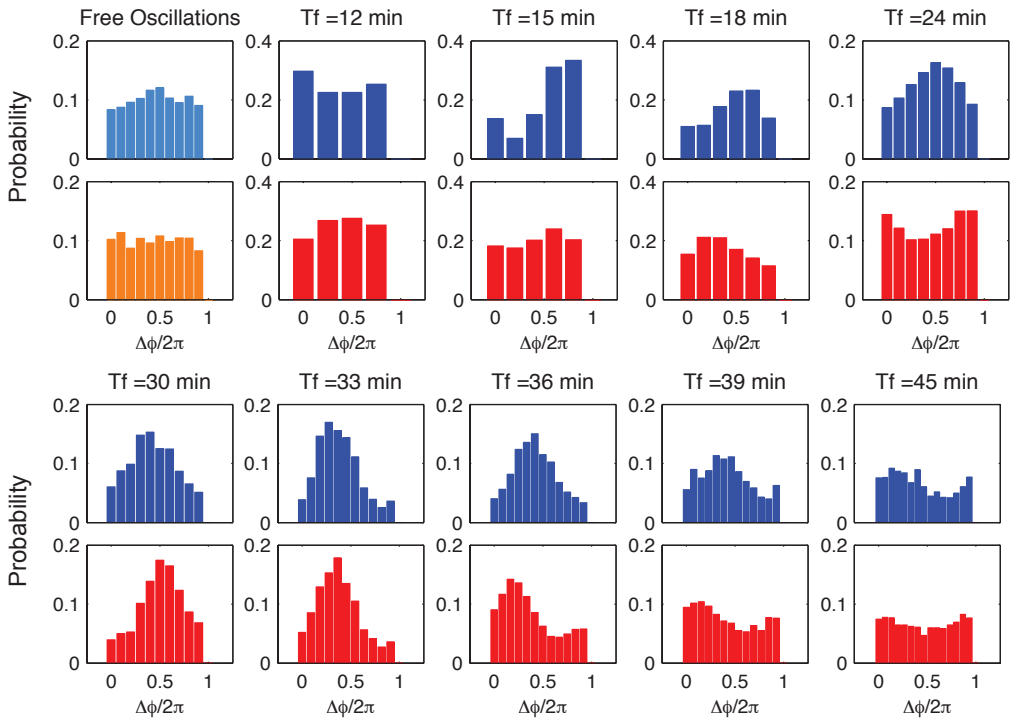

Fig. S2: Comparison of the experimental (blue) and stochastic model (red) probability distributions of the normalized relative phase $\Delta\phi/2\pi$ for a forcing amplitude A =0.075 %.

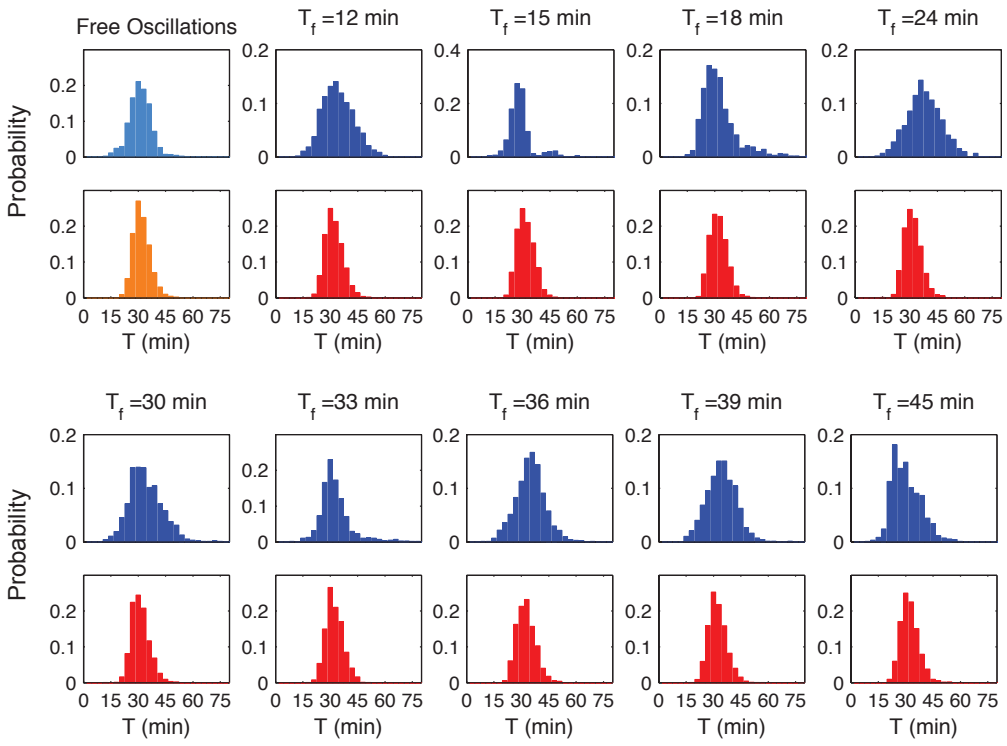

Fig. S3: Comparison of the experimental (blue) and stochastic model (red) probability distributions of the period T for a forcing amplitude A =0.075 %.

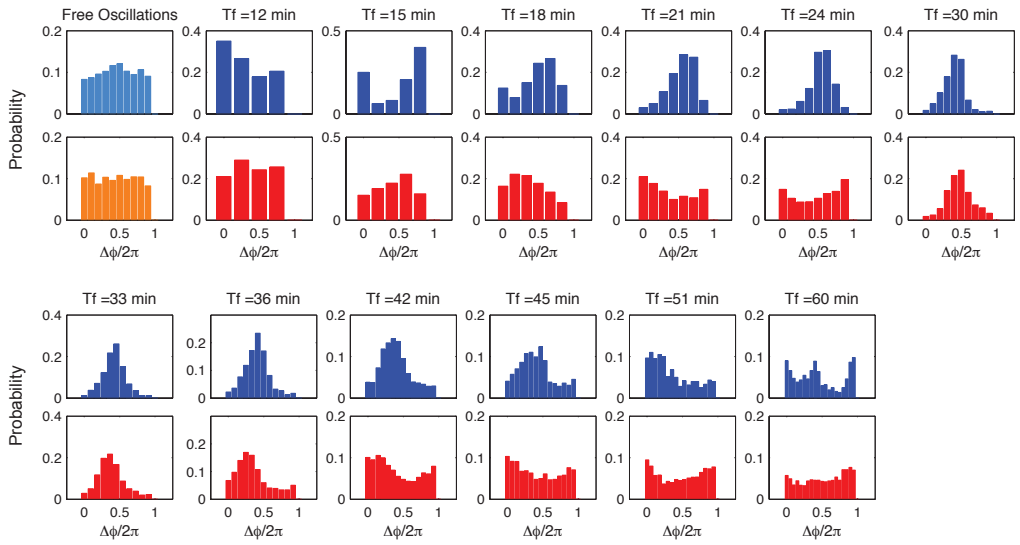

Fig. S4: Comparison of the experimental (blue) and stochastic model (red) probability distributions of the normalized relative phase $\Delta\phi/2\pi$ for a forcing amplitude A =0.15 %.

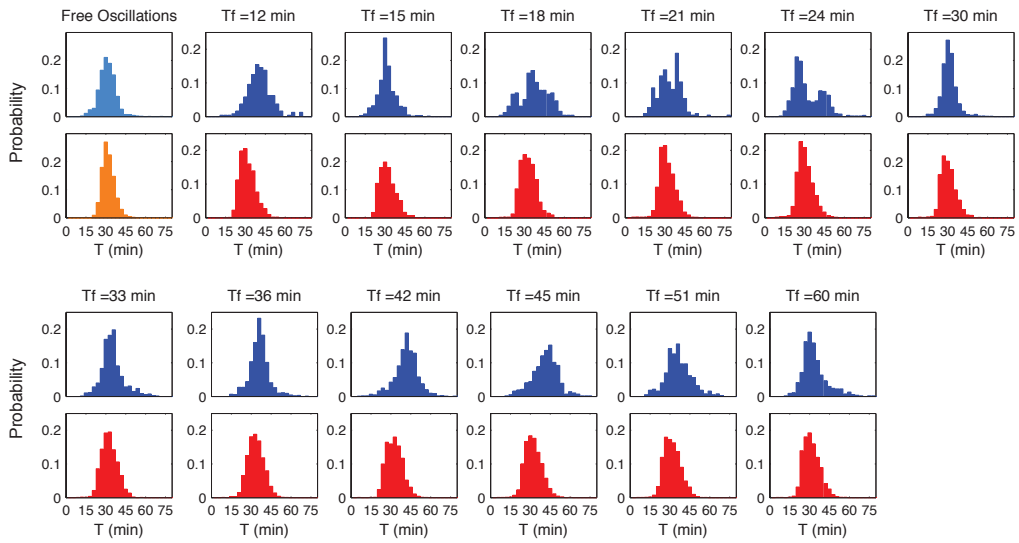

Fig. S5: Comparison of the experimental (blue) and stochastic model (red) probability distributions of the period T for a forcing amplitude A =0.15 %.

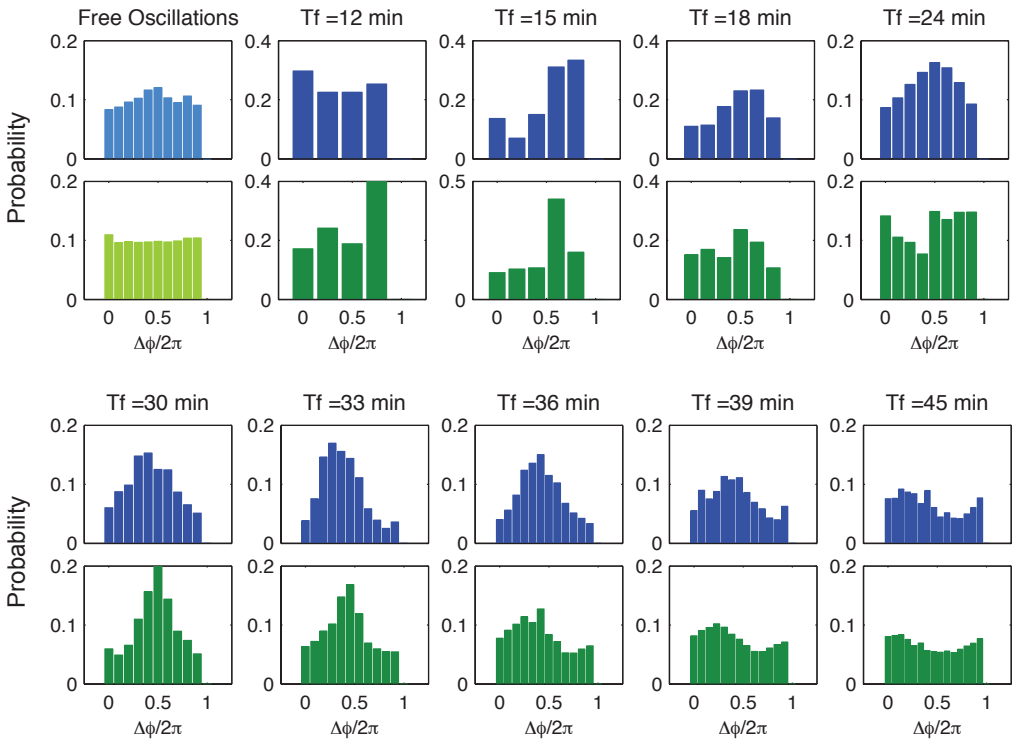

Fig. S6: Comparison of the experimental (blue) and deterministic (green) probability distributions of the normalized relative phase $\Delta\phi/2\pi$ for a forcing amplitude A =0.075 %.

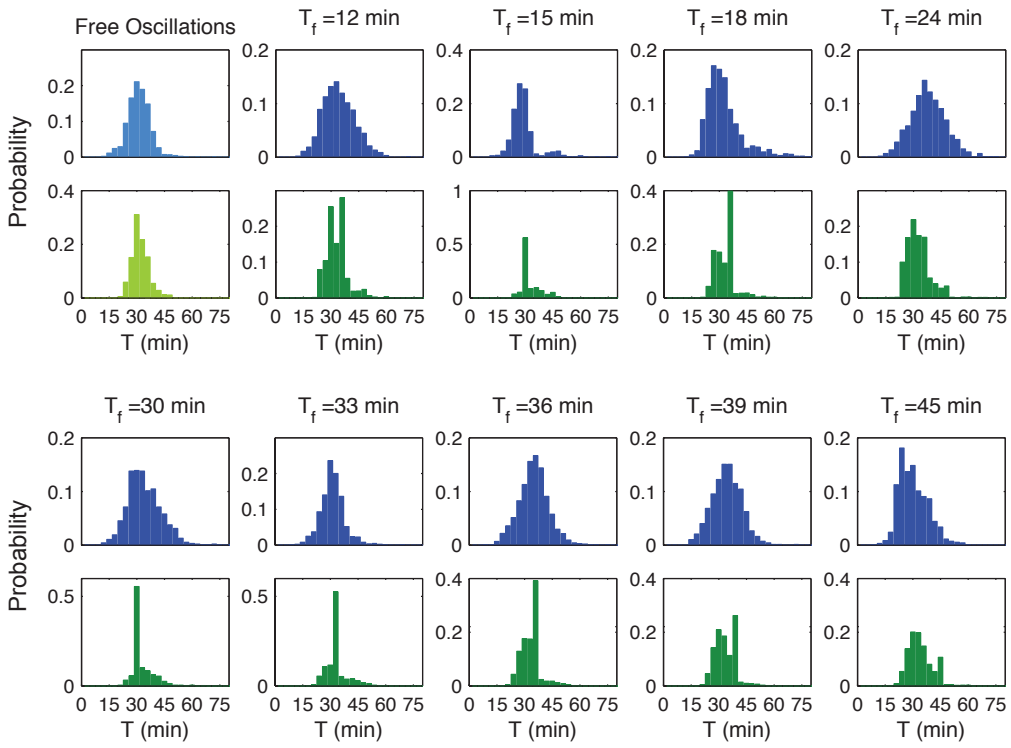

Fig. S7: Comparison of the experimental (blue) and deterministic (green) probability distributions of the period T for a forcing amplitude A =0.075 %.

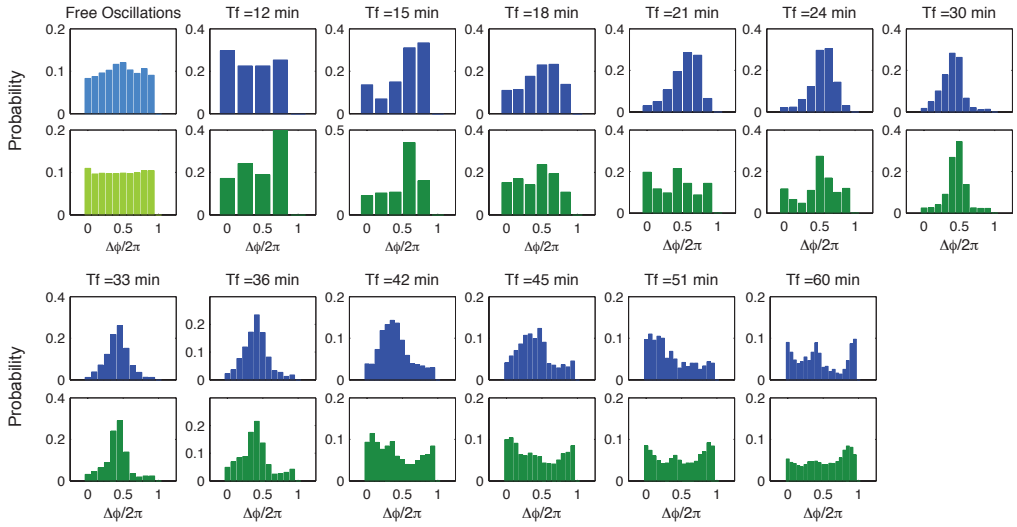

Fig. S8: Comparison of the experimental (blue) and deterministic (green) probability distributions of the normalized relative phase $\Delta\phi/2\pi$ for a forcing amplitude A =0.15 %.

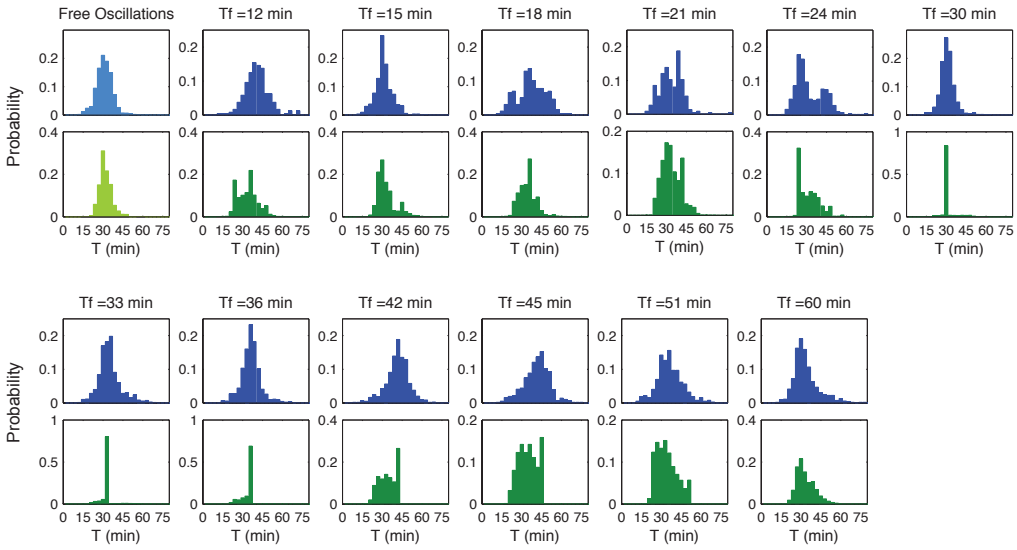

Fig. S9: Comparison of the experimental (blue) and deterministic (green) probability distributions of the period T for a forcing amplitude A =0.15 %.

Movie S1. Time lapse fluorescence microscopy of JS011 cells in a microfluidic chamber subject to a sinusoidally changing concentration of arabinose with average [ara] = 0.3 %, amplitude A = 0.15 % and period Tf = 30 min, and constant IPTG concentration 2 mM. The GFP and MCherry fluorescence are shown in green and red respectively, the phase contrast image is shown in grey. Total time of the movie is 300 min with a sampling rate of one image every 3 min.

Movie S2. Time lapse fluorescence microscopy of JS011 cells in a microfluidic trap at constant inducer concentrations [ara] = 0.3 % and [IPTG] = 2 mM. The GFP and MCherry fluorescence are shown in green and red respectively, the phase contrast image is shown in grey. Total time of the movie is 360 min with a sampling rate of one image every 3 min.

Movie S3. Time lapse fluorescence microscopy of JS011 cells in a microfluidic chamber subject to a sinusoidally changing concentration of arabinose with average [ara] = 0.3 %, amplitude A = 0.075 % and period Tf =30 min, and constant IPTG concentration 2 mM. The GFP and MCherry fluorescence are shown in green and red respectively, the phase contrast image is shown in grey. Total time of the movie is 372 min with a sampling rate of one image every 3 min.

Movie S4. Time lapse fluorescence microscopy of JS011 cells in a microfluidic chamber subject to a sinusoidally changing concentration of arabinose with average [ara] = 0.3 %, amplitude A = 0.075 % and period Tf = 15 min, and constant IPTG concentration 2 mM. The GFP and MCherry fluorescence are shown in green and red respectively, the phase contrast image is shown in grey. Total time of the movie is 300 min with a sampling rate of one image every 3 min.

Movie S5. Time lapse fluorescence microscopy of JS011 cells in a microfluidic chamber subject to a sinusoidally changing concentration of arabinose with average [ara] = 0.3 %, amplitude A = 0.15 % and period Tf = 15 min, and constant IPTG concentration 2 mM. The GFP and MCherry fluorescence are shown in green and red respectively, the phase contrast image is shown in grey. Total time of the movie is 300 min with a sampling rate of one image every 3 min.

Movie S6. Example of the cell tracking algorithm applied to E. coli bacteria in a microfluidic chamber described in the supporting online text. Top left panel shows the capability of our algorithm to track three individual cells using bright field images. The top right panel shows fluorescence profiles extracted from the fluorescence images. The bottom plot shows the fluorescent trajectories corresponding to the average fluorescence value for each cell.